Wideband dielectric metamaterial reflectors: Mie scattering or leaky Bloch mode resonance?: supplementary material
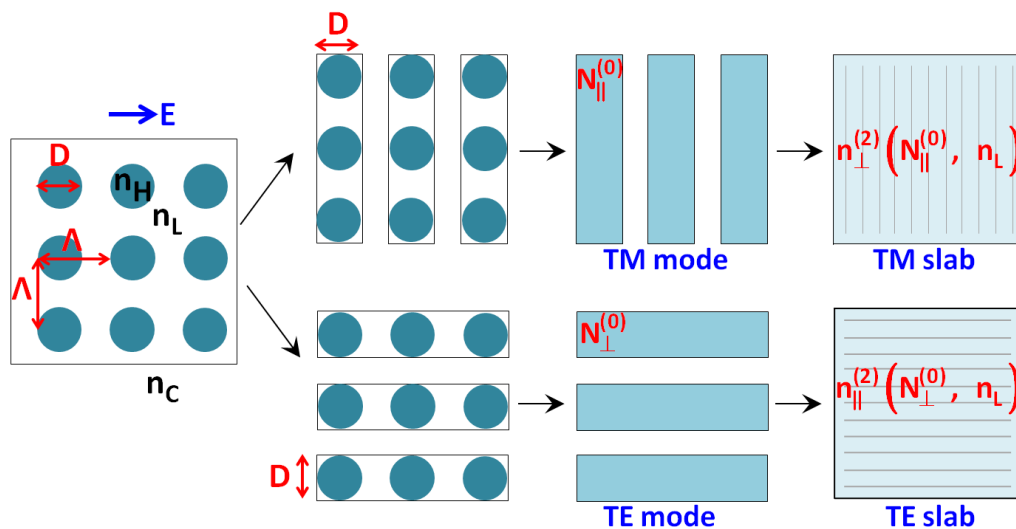
YEONG HWAN KO AND ROBERT MAGNUSSON[*]

Department of Electrical Engineering, University of Texas at Arlington, Box 19016, Arlington, Texas 76019, USA

Corresponding author: magnusson@uta.edu

This document provides supplementary information to "Wideband dielectric metamaterial reflectors: Mie scattering or leaky Bloch mode resonance?," https://doi.org/10.1364/OPTICA.5.000289. Here, we explain further details on simulation and modeling. Section 1 presents the effective medium conversion of a 2D resonant lattice to 1D slab waveguide. In conversion to 1D from 2D, Section 2 shows the modal processes with two equivalent 1D models. Section 3 illustrates the discussion of Mie scattering in isolated Si rods. Finite-difference time-domain (FDTD) simulations are employed to quantify the total scattering cross section (TSCS) spectra of an isolated Si rod. Utilizing an enclosed launch excitation type, only scattered fields outside the launch boundary are numerically encountered. Section 4 explains the specific boundary conditions in the FDTD simulations to make the four visualizations of the electrodynamics of light propagation in periodic and finite Si gratings.

1. Effective Medium Conversion

Figure S1. Effective-medium conversion of a 2D resonant lattice to 1D slab representations. Using the zero-order effective index, the 2D constituent grating is decomposed into two quasi-equivalent 1D grating components, where TM and TE modes have their electric-field vectors perpendicular and parallel to the grooves of the 1D grating. Then, the two equivalent 1D-slab waveguide structures are modeled using the second-order effective index.

To enable clear understanding of the physics governing resonant lattices, we decompose the 2D lattice into quasi-equivalent 1D lattices. As depicted in Fig. S1, the corresponding 1D gratings are established by zero-order effective-medium theory (EMT) given by

$$N_{\parallel}^{(0)} = \left[Fn_H^2 + (1-F)n_L^2 \right]^{1/2} \ and$$

$$N_{\perp}^{(0)} = \left[Fn_H^{-2} + (1-F)n_L^{-2} \right]^{-1/2} \quad \textbf{(S1)}$$

$$where \ F = \pi D / 4\Lambda$$

Then, two equivalent 1D-slab structures are converted from each 1D TM and TE grating component (see definition in Fig. S1) using second-order EMT [1,2]. Therefore, the TM and TE slab structures have second-order effective indices $n_{\perp}^{(2)}\left(N_{\parallel}^{(0)}, n_L\right)$ and $n_{\parallel}^{(2)}\left(N_{\perp}^{(0)}, n_L\right)$ that are given by the following functions of $n_{\perp}^{(2)}(a,b)$ and $n_{\parallel}^{(2)}(a,b)$.

$$n_{\parallel}^{(2)}(a,b) = \left[\left(n_{\parallel}^{(0)}(a,b) \right)^2 + \left(\frac{\Lambda}{\lambda} \right)^2 C_{\parallel}(a,b) \right]^{1/2} \ and$$

$$n_{\perp}^{(2)}(a,b) = \left[\left(n_{\perp}^{(0)}(a,b) \right)^2 + \left(\frac{\Lambda}{\lambda} \right)^2 C_{\perp}(a,b) \right]^{1/2} \quad \textbf{(S2)}$$

$$C_{\parallel}(a,b) = \frac{1}{3}\pi^2 f^2 (1-f)^2 \left(a^2 - b^2 \right)^2 \ and$$

$$C_{\perp}(a,b) = \frac{1}{3}\pi^2 f^2 (1-f)^2 \left(\frac{1}{a^2} - \frac{1}{b^2} \right)^2 \left(n_{\perp}^{(0)} \right)^6 \left(n_{\parallel}^{(0)} \right)^2 \quad \textbf{(S3)}$$

$$where \ f = D / \Lambda$$

$$n_{\parallel}^{(0)}(a,b) = \left[fa^2 + (1-f)b^2 \right]^{1/2} \ and$$

$$n_{\perp}^{(0)} = \left[fa^{-2} + (1-f)b^{-2} \right]^{-1/2} \quad \textbf{(S4)}$$

where $n_{\parallel}^{(2)}(a,b)$ and $n_{\perp}^{(2)}(a,b)$ are the second-order effective indices as functions of two different indices (a,b). The $C_{\parallel}(a,b)$ and $C_{\perp}(a,b)$ are constant coefficient multipliers for TE and TM polarizations as seen in Eq. (3). The $n_{\parallel}^{(0)}$ and $n_{\perp}^{(0)}$ are the effective indices in the zero-order EMT approximation for decoupled two 1D grating structures. To calculate the modal curves using the estimated effective index, we used the classic formulas[3] for the slab structure in air (n_c=1) as follows

$$tan\left[\kappa_i(\lambda)d \right] = \frac{\left[\gamma_i(\lambda) + \delta_i(\lambda) \right] \kappa_i(\lambda)}{\kappa_i^2 - \gamma_i(\lambda)\delta_i(\lambda)} \quad (TE)$$

$$tan\left[k_i(\lambda)d \right] = \frac{n_{slab}^2 \left[n_c^2\gamma_i(\lambda) + n_c^2\delta_i(\lambda) \right] \kappa_i(\lambda)}{n_c^4\kappa_i^2(\lambda) - n_{slab}^4\gamma_i(\lambda)\delta_i(\lambda)} \quad (TM) \quad \textbf{(S5)}$$

where $\kappa_i(\lambda) = \left(n_{slab}^2 k^2 - \beta_i^2(\lambda) \right)^{1/2}$,

$\gamma_i(\lambda) = \left(\beta_i^2(\lambda) - n_C^2 k^2 \right)^{1/2}$, $\delta_i(\lambda) = \left(\beta_i^2(\lambda) - n_c^2 k^2 \right)^{1/2}$
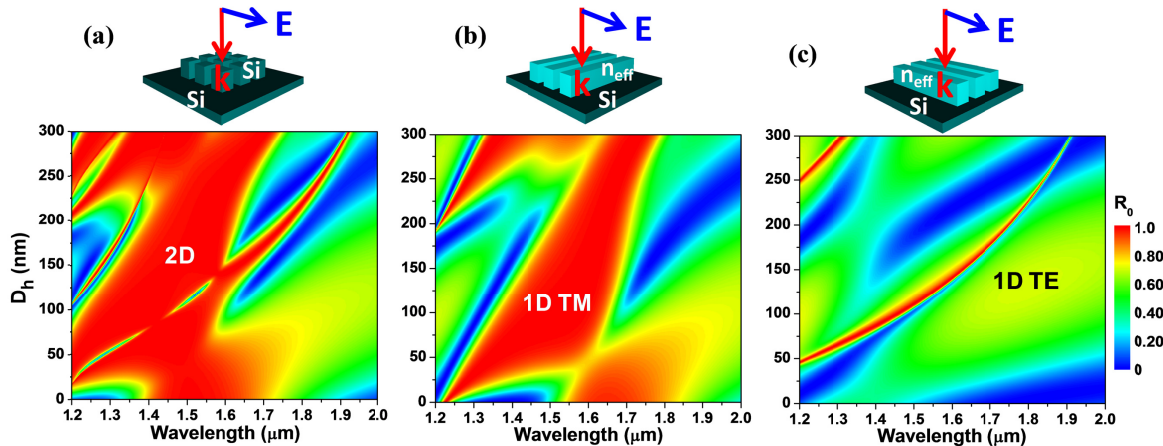
Here the estimated effective refractive index is applied for each slab waveguide by $n_{slab}(TE) = n_{\parallel}^{(2)}\left(n_{\parallel}^{(0)}, n_L\right)$ and $n_{slab}(TM) = n_{\perp}^{(2)}\left(n_{\perp}^{(0)}, n_L\right)$. The propagation constant is then defined as an effective propagation constant β_i

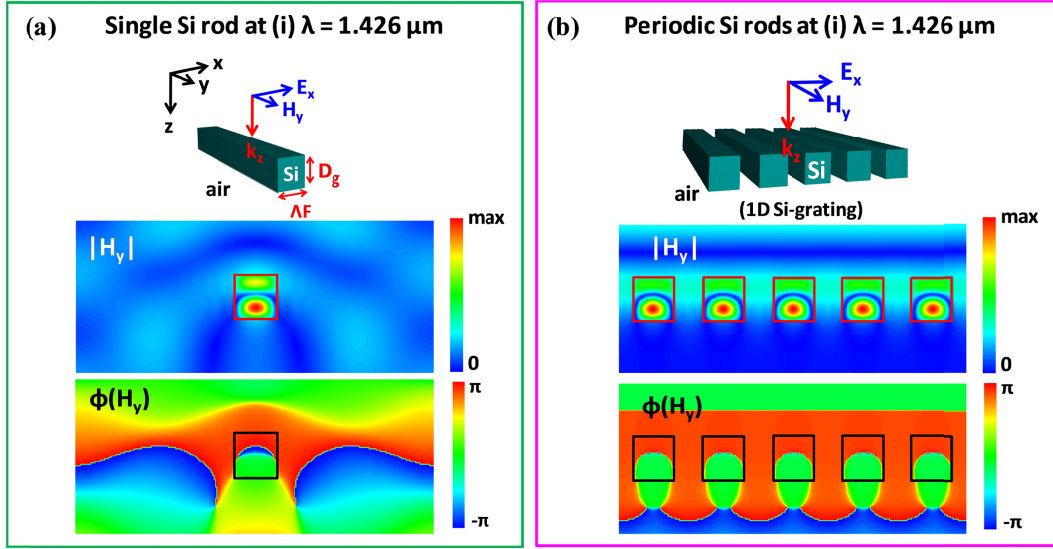$$\beta_i(\lambda) = k\left(n_{slab}sin(\theta) - i\lambda/\Lambda \right) \quad \textbf{(S6)}$$

with grating period Λ and angle of incidence θ. The i integers label the diffracted waves. Finally, the slab waveguide modes as a function of the slab thickness d are characterized for the TE and TM modes.

2. Equivalent 1D Models

In the conversion to 1D, we approximate the cylindrical pillars by square pillars having the same diameter and height. Comparing the reflectance spectra of Fig. 2(b) main text (cylindrical pillars) to the spectra in Fig. S2(a) (square pillars) shows that this is a good approximation. Utilizing second-order effective-medium theory (2nd EMT) [2], we reduce the dimension of the 2D grating into two quasi-equivalent 1D gratings. The 1D gratings are orthogonal to each other and they have TM and TE effective refractive index calculated by 2nd EMT. The detailed method is explained in a previous paper.[4] From the R_0 maps in Figs. S2(b) and S2(c), it is seen that all main reflectance features of the 2D grating originate from a blend of TM and TE resonant leaky modes. It is notable that the TM modes contribute the broad band of high reflection. Degraded reflection appears where the TM and TE modes coexist in the 2D grating. Optimization of the 2D resonant reflector should be implemented to avoid the degraded reflection zone.

Figure S2 Modal processes in 2D guided-mode resonant lattices and correlations with processes in effective 1D decompositions. The R_0 color maps as a function of D_h are displayed for (a) the original 2D rectangular grating, (b) 1D TM polarized reflector, and (c) 1D TE polarized reflector. The complex modal processes in the 2D resonant grating are explainable by more transparent processes occurring in the 1D resonant gratings.
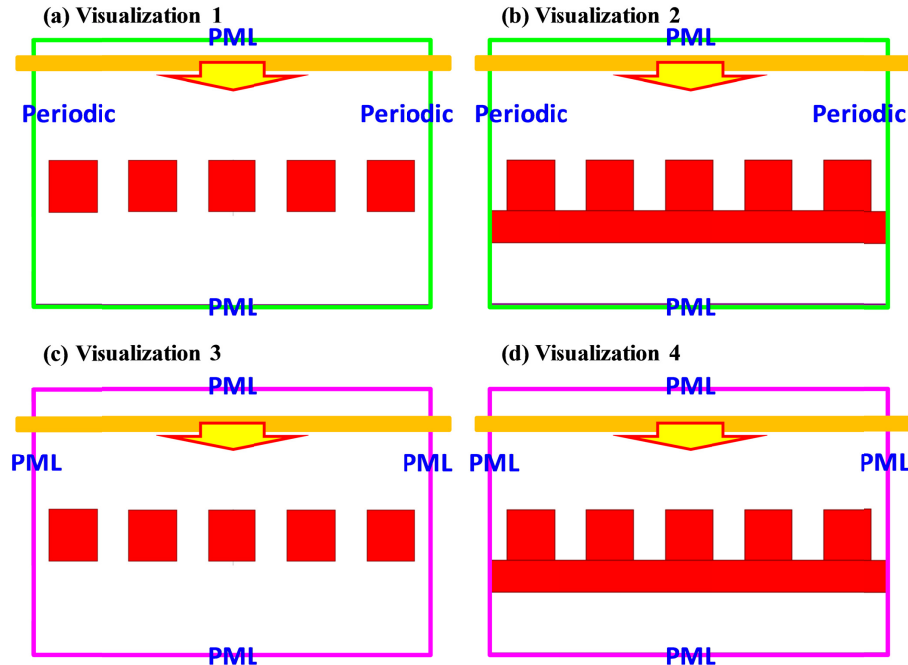
Figure S3 Mie scattering and guided-mode resonance in relation to the 1D Si grating in Fig. 3(c) of the main text. Magnitude and phase of field distribution in (a) a single Si rod and in a (b) periodic Si grating at same wavelength (i) 1.426 μm.

3. Mie Scattering In Isolated Rods

Figure S3 shows the comparison of field distributions in single and periodic Si rods at wavelengths (i) 1.426 μm as marked in Fig. 4(b) of the main text. Notably, the electric dipole field signature in the single Si rod of Fig. S3(a) does not maintain as the rods are periodically arranged to enter the guided-mode resonance regime. As displayed in Fig. S3(b), the localized field and phase profiles are significantly different from the Mie resonance profile of the single Si rod even at the Mie electric-dipole wavelength. In fact, the profile at λ = 1.426 μm is close to the field distribution associated with counterpropagating lateral Bloch modes as provided in Fig. 3(c) (main text).

4. Numerical Visualizations

We visualize the dynamic field distributions in the Si-grating reflector by recording FDTD simulations with different boundary conditions as shown in Fig. S4. The reflector without (a) and with (b) a sublayer is modeled using periodic boundary conditions at the lateral sides of the simulation boundary. We remove scattering at the top and bottom boundaries with perfectly matched layers (PMLs). To eliminate counterpropagation and standing waves, finite grating reflectors without (c) and with (d) a sublayer are modeled by the PMLs at the sides of simulation boundary as noted in Fig. S4.

Figure S4 Arrangement of simulation boundaries for recording the dynamic resonant fields. The reflector without (a) and with (b) a sublayer is modeled using periodic boundary conditions at both sides of the simulation boundary. Finite grating reflectors without (c) and with (d) a sublayer are modeled with PMLs at both sides of the simulation boundary.

References

1. R.Bräuer and O. Bryngdahl, "Design of antireflection gratings with approximate and rigorous methods," Appl. Opt. **33**, 7875-7882 (1994)

2. D. L.Brundrett, E. N. Glytsis, and T. K. Gaylord, "Homogeneous layer models for high-spatial-frequency dielectric surface-relief gratings: Conical diffraction and antireflection designs," Appl. Opt. **33**, 2695–2706 (1994).

3. S. S. Wang and R. Magnusson, "Theory and applications of guided-mode resonance filters," Appl. Opt. **32**, 2606-2613 (1993).

4. Y. H. Ko, M. Shokooh-Saremi, and R. Magnusson, "Modal processes in two-dimensional resonant reflector and their correlation with spectra of one-dimensional equivalents," IEEE Photon. J. **7**, 4900210 (2015).